The Thesis Committee for Samantha J. Fuchs
Certifies that this is the approved version of the following thesis:

Geochemical and Geomechanical Alteration of Mt. Simon Sandstone due to Prolonged Contact with CO_2-saturated Brine during Carbon Sequestration

APPROVED BY
SUPERVISING COMMITTEE:

Supervisor:

Charles J. Werth

Lynn E. Katz

Geochemical and Geomechanical Alteration of Mt. Simon Sandstone due to Prolonged Contact with CO_2-saturated Brine during Carbon Sequestration

by

Samantha J. Fuchs, B.S.

Thesis

Presented to the Faculty of the Graduate School of

The University of Texas at Austin

in Partial Fulfillment

of the Requirements

for the Degree of

Master of Science in Engineering

The University of Texas at Austin

May 2017

Acknowledgements

This work was supported as part of the Center for Geological Storage of CO_2, an Energy Frontier Research Center funded by the U.S. Department of Energy, Office of Science. Data for this project were provided, in part, by work supported by the U.S. Department of Energy under award number DE-FC26-05NT42588 and the Illinois Department of commerce and Economic Opportunity.

I would like to thank my supervisor, Dr. Charles Werth, for his help and guidance throughout the course of my research and writing. I am lucky to have learned so much and to continue to do so in the future. I also want to thank Julien Botto, my laboratory partner who did the foundational work on this research before his graduation.

I would like to thank Michael Aman and Dr. Nicholas Espinoza of Petroleum and Geosystems Engineering at UT Austin for assistance and training on geomechanical testing. I would like to thank Dr. Mark Cloos and Jaspal Singh from the Jackson School of Geosciences for their technical recommendations and assistance with geology equipment training. I would like to thank Dr. Dustin Crandall, of NETL, and Dr. Ange Akono, of UIUC, for being friendly and helpful in providing context for my work within the GSCO2 Center. I would like to thank Dr. Lynn Katz for being on my committee. Finally, I would like to thank Daryl Nygaard and Phil Tomlin, both masters of their respective machine shops, who were always available to help with my experimental equipment.

Much love and thanks to my family and friends who provided me emotional support as I talked about rocks non-stop for a year.

Abstract

Geochemical and Geomechanical Alteration of Mt. Simon Sandstone due to Prolonged Contact with CO_2-saturated Brine during Carbon Sequestration

Samantha J. Fuchs, M.S.E.

The University of Texas at Austin, 2017

Supervisor: Charles J. Werth

Geologic carbon sequestration is an emerging approach for mitigating climate change due primarily to point-source CO_2 emissions. Sequestration of carbon dioxide in deep saline aquifers prevents the release of CO_2 to the atmosphere. The Mt. Simon formation in the Illinois Basin is the site of a pilot-scale geologic carbon sequestration effort. It is a siliciclasic formation consisting of primarily quartz and potassium feldspar, cemented by illite-smectite and iron-illite clays. During CO_2 injection, carbon dioxide dissolves into pore water, resulting in a low-pH brine that can dissolve clays, carbonates, and other reactive minerals. In this work, the geochemical reactions resulting from the

interaction of acidified-brine and reservoir rock are probed during and after aging samples of Mt. Simon sandstone in CO_2-saturated brine under reservoir conditions. During aging, contact angle measurements of supercritical CO_2 suggest the loss of iron-illite and increase of surface roughness. Post-aging, scanning electron microscopy coupled with electron dispersive spectroscopy revealed the loss of clays, greater exposure of quartz and K-feldspar grains, and apparent roughening, confirmed by XRD analysis and laser profilometer surface images respectively. Scratch tests were performed on both unaltered and aged samples, and the latter show a 63% decrease in fracture toughness. I conclude that acidified brine causes dissolution of clays and K-feldspar during carbon sequestration that weakens the Mt. Simon sandstone matrix along quartz and feldspar grain boundaries. This process may contribute to microseismic activity observed at the Mt. Simon sequestration site during and after CO_2 injection.

Table of Contents

List of Figures

List of Tables

Introduction

Carbon dioxide is a potent greenhouse gas that is a direct cause of anthropogenic climate change. Since the 1950s, observed climate changes have occurred at unprecedented rates, resulting in high carbon dioxide concentrations in the atmosphere, sea level rise, loss of snow and ice, and severe weather events of increasing frequency (IPCC, 2014). In 2014, greenhouse gas emissions from the United States totaled 6,870 million metric tons (6,870,000,000 Mt) of carbon dioxide equivalents, of which 82% was carbon dioxide (US EPA, 2016). Although many renewable energy sources are being implemented that produce low carbon emissions, the United States and many industrialized countries rely predominantly on petroleum products like oil and natural gas for fuel. Additionally, construction relies on cement production and the iron and steel industry, which contribute 932 and 646 $MtCO_2$ per year, respectively (IPCC, 2005). Trapping and storing carbon dioxide to prevent it from entering the global carbon cycle is an essential mitigation technique to prevent further rise of atmospheric CO_2 and unknown climate effects.

Geologic carbon sequestration is a method wherein carbon dioxide is trapped at a stationary source, such as a power plant or a refinery, and then injected deep underground for long-term storage via structural trapping, capillary trapping, dissolution into pore water, and/or mineralization. Three primary storage locations have been proposed for geologic carbon sequestration: deep saline formations, oil and gas fields, and unmineable coal beds. The lower estimate of storage capacity for these reservoirs are 1000, 675, and 3-15 $GtCO_2$ respectively (IPCC, 2005). Upper estimates of storage capacity for deep

saline formations are as high as 10,000 $GtCO_2$ worldwide—much greater than those for oil and gas fields and unmineable coal beds. This makes them the most promising option for large-scale sequestration of CO_2 from stationary sources.

A key knowledge gap hindering the development of geological carbon sequestration in deep saline formations is the impact of geochemical reactions between CO_2, brine, and reservoir rock on geomechanical properties. Geochemical reactions can weaken reservoir rock, potentially leading to small fractures that propagate and impact CO_2 migration pathways or cap rock integrity. Multiple studies have investigated geochemical reactions between CO_2, brine and reservoir rocks, using both static batch and dynamic core-flood experiments (Czernichowski-Lauriol et al., 2006). The primary type of reaction is dissolution due to the lowered pH of brine after CO_2 injection. Particularly reactive mineral end members like calcite or dolomite readily dissolve in low pH solutions (Deng, Fitts, Crandall, McIntyre, & Peters, 2015; X. Wang, Alvarado, Swoboda-Colberg, & Kaszuba, 2013). Additional minerals such as hematite, K-feldspar, and clays like illite and smectite, dissolve, but at slower rates depending on temperature (Amram & Ganor, 2005; Rosenqvist, Kilpatrick, Yardley, & Rochelle, 2014; Wigley, Dubacq, Kampman, & Bickle, 2013). These different individual reactions occur in tandem within heterogeneous reservoir rock samples, but can have compounded effects due to precipitation of weathering byproducts as clays (Wigand, Carey, Schütt, Spangenberg, & Erzinger, 2008). The implications of these geochemical reactions on geomechanical properties have received considerably less attention. There have been

numerous studies on either geochemistry or geomechanical properties of reservoir materials, but a lack of studies integrating these together (Dawson et al., 2013).

The objectives of my thesis are to study the geochemical reactions that occur in a representative siliciclastic storage reservoir during CO_2 sequestration and determine if these reactions weaken reservoir rock and make it more prone to fracturing and induced seismic events. The Mt. Simon formation was chosen as a typical siliciclastic reservoir for study; it is the site of a pilot CO_2 injection project, where 1 million metric tons of CO_2 was injected between 2011 and 2014 (Kaven, Hickman, Mcgarr, & Ellsworth, 2015). The mineralogy of the Mt. Simon sandstone includes quartz, potassium feldspar, illite, iron oxide-illite, and illite-smectite, which comprise 99.31% of the formation (Freiburg, Morse, Leetaru, Hoss, & Yan, 2014). Samples of the Mt. Simon sandstone were aged in CO_2-saturated brine at reservoir conditions, 60°C and 20 MPa (2900psi). During aging, the contact angle of CO_2 on the sandstone surface was monitored as a surrogate for geochemical reactions altering the surface chemistry and structure. Before and after sample aging, optical microscopy, scanning electron microscopy (SEM), energy dispersive spectroscopy (EDS), and laser profilometry were used to quantify changes in surface mineralogy and roughness. X-ray diffraction (XRD) was used to quantify changes in bulk mineralogy. Geomechanical tests were performed to measure changes in sample fracture toughness and scratch hardness, which were related to changes in sample mineralogy. The effects on geomechanical properties due to aging on potential microseismicity are explored.

Materials and Methods

Materials

Liquid CO_2 (99.5% purity, Praxair) was used for all experiments. Synthetic brine was composed of nanopure water (18 MΩ·cm) and sodium chloride (Alfa Aesar, 99%), calcium chloride (Sigma Aldrich, 99%), magnesium chloride (Sigma Aldrich, 99%), potassium chloride (MP Biomedicals, 99%), potassium bromide (Alfa Aesar, 99%), lithium chloride (Alfa Aesar, 99.9%), strontium chloride (Strem Chemicals, %), and borax (MP Biomedicals, 99%). The synthetic brine recipe is based on the Mt. Simon formation pore water and is given in Table A1.

Rock Core and Sample Preparation

A Mt. Simon core sample, 3 in length, 1 in diameter, was obtained from the Illinois Basin Decatur site under the direction of the Geological Sequestration Consortium. It is a sidewall core sample from Verification Well #1 at a depth of 6726 ft (2050.09 m). The mineralogical make-up of the lower Mt. Simon formation was previously determined using scanning electron microscopy (SEM) coupled to energy dispersive spectroscopy (EDS). The minerals include quartz, potassium feldspar (K-feldspar), illite, iron oxide-illite, and illite-smectite, which comprised 99.31% of the formation (Freiburg et al., 2014). The mineralogical composition of Mt. Simon sandstone material from the same depth interval as the sidewall core used in this study was also evaluated (Botto et al., 2017), and agrees with Freiburg et al. (2014). Note that the CO_2 injection zone is 6984-7050 ft (2128-2148 m) (Freiburg et al., 2014), so no CO_2

contact with the sidewall core material occurred from injection.

The sidewall core was cut using a low speed diamond wheel saw (South Bay Technology Inc., Model 650) with a 10:1 dilution of deionized water to lubricant oil (Johnson Brothers, Lube Cool, LC-16). Samples were cut into 1 in diameter, and either 1/8 in thick or ¾ in thick disk samples. The 1/8 in sample was aged in CO_2 saturated brine in a view cell (as described below) and contact angle measurements were performed over time as a surrogate measure of geochemical changes; contact angle measurements on a similar sample showed they are a function of surface mineralogy and roughness (Botto et al., 2017), both of which may change with aging. The thicker sample was not aged, but was used only for destructive geomechanical experiments. After cutting, all disk samples were rinsed for five minutes with ethanol (ACS grade, Pharmco-Aaper), and dried in an oven for 24 hours at 50°C.

Thin sections (30 μm thick) of sidewall core material were prepared by the Thin Section Laboratory at the Jackson School of Geosciences at UT Austin before and after sample aging to evaluate changes in mineralogy. The sandstone was vacuum impregnated with blue epoxy (EpoThin Epoxy Hardener and Resin, Bueller) to aid in identification of pore spaces versus mineral grains. The resin was cured for four hours in an oven at 60°C. After cooling, the sample surface was polished with a 70 μm abrasive disc, and then a 10 μm polishing disc, both on a geologic grinder-polisher (MetaServ 250, Bueller). Final polishing was done with 600 grit Al_2O_3 (Bueller) in kerosene (1K Heater Fuel) on a glass plate before washing with isopropyl alcohol (IUPAC name propan-2-ol, Pharmco-Aaper, ACS grade). The polished thin section was then bonded, polished side down, to a glass

slide with UV-activated epoxy (EpoFix Hardener and Resin, Struers), and cured for 60 seconds under a UV light. Remaining epoxy and sample was cut with a diamond saw and grinder to reduce the thin section to 50 μm. Fine polishing to 30 μm was done in three steps; first with the 10 μm polishing disc on the lapping machine, then on the glass plate with 600 grit Al_2O_3 in kerosene, and finally with 1000 grit Al_2O_3 in kerosene. This was followed by washing with isopropyl alcohol and air drying.

High Pressure and Temperature View Cell Setup

Sample aging and contact angle measurements were performed in a custom-built high-pressure and temperature view cell illustrated in Figure 1. As described in previous research (Botto et al., 2017; S. Wang, Edwards, & Clarens, 2013), the view cell is a stainless-steel hollow cylinder with an outer diameter of 3.8 in and an inner diameter of 1, rated to 10,000 psi (69 MPa). The interior volume is 20 mL, sealed with two Teflon O-rings and two sapphire windows held in place with threaded rings on either end. There are four ports spaced equally around the cylinder for brine introduction, pressure release, CO_2 injection, and a pressure safety head (HIP). There is one thermocouple well set near the top port. Within the view cell, a custom glass holder, 1.5 in long by 1 in diameter, holds the sample in place. The view cell is held horizontally on an L-shaped stainless steel stage and set level by four adjustable screws on a Solid Aluminum Optical Breadboard (Newport).

The experimental setup is shown in Figure 2. The liquid CO_2 tank was connected to a Teledyne Isco pump (Model 100DM). The pump injected liquid CO_2 into an HIP

stainless-steel reactor (HIP OC-3 Series) for pre-equilibration of CO_2 with brine, and into the view cell to maintain pressure and introduce CO_2 bubbles for contact angle measurement. Heating tape (Briskheat BIH051020L) was wrapped around the view cell, and wrapped in woven silica coated in flexible aluminized finish (ThermoTec aluminized heat barrier). Two Omega-K type thermocouples were used to measure the temperature of the heating tape and the view cell. The heating tape and thermocouples were monitored and controlled by a National Instrument Data Acquisition (NIDAQ) system and Labview software.

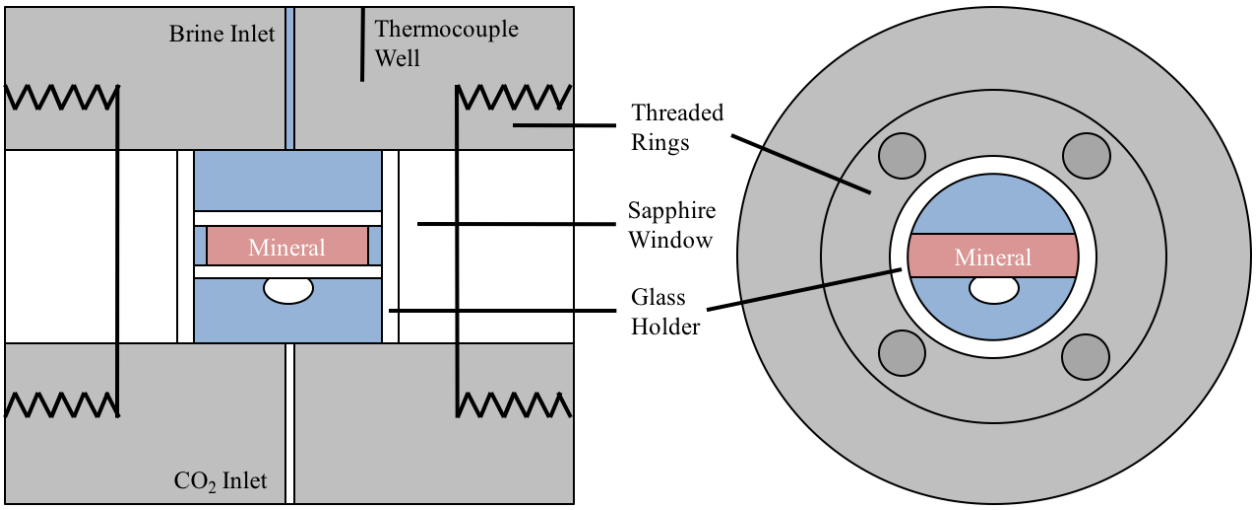

Figure 1: View Cell Schematic from bisected side view (left) and front view (right).

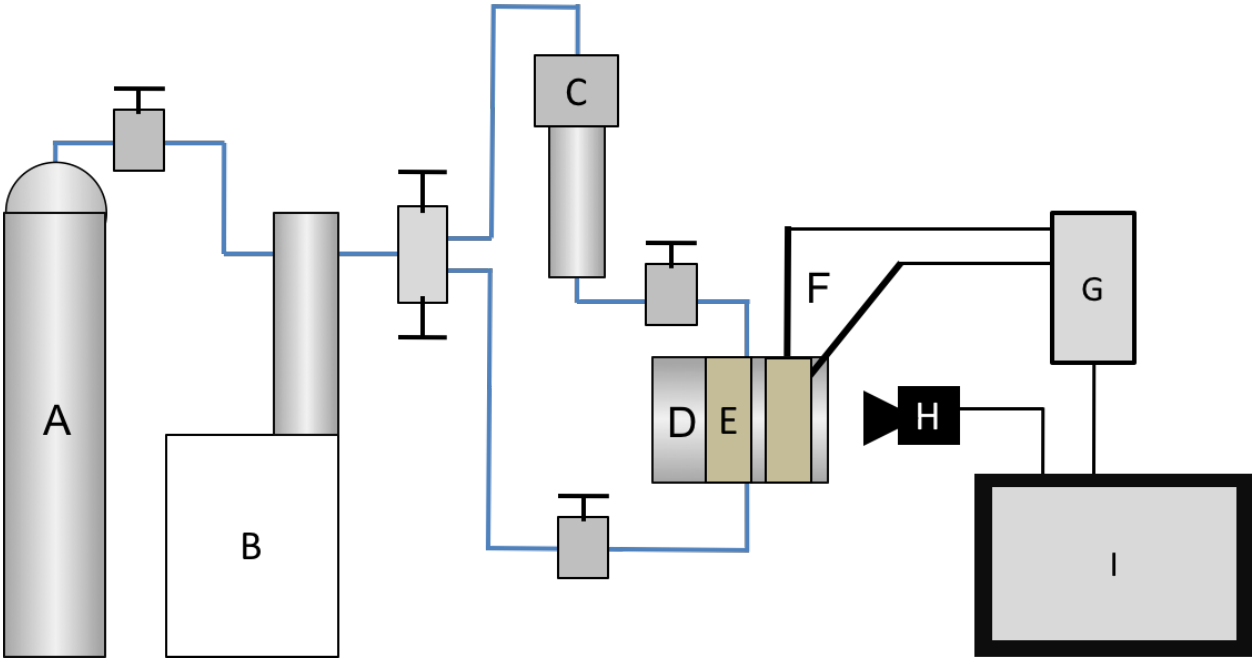

Figure 2: Experimental Set-Up Diagram.

A: Liquid CO_2 Cylinder; B: ISCO Pump; C: Brine-CO_2 Equilibrium Reactor; D: View Cell; E: Heating Tape; F: Internal and External Thermocouples; G: National Instruments (MODEL), H: Time lapse camera; I: Labview Control Computer.

Sample Aging and Contact Angle Methods

For each aging experiment, a sample was put into the glass holder and placed in the open view cell. The ends were sealed by Teflon O-rings that sit against the sapphire windows. The view cell was first flushed with CO_2 to remove oxygen, heated to 60°C, and then filled with pre-equilibrated brine from the HIP stainless steel reactor. The ISCO pump (i.e., constant pressure control) was used to inject supercritical CO_2 over 45

minutes to reach 2900 psi (20 MPa). The selected temperature and pressure are similar to those in the Mount Simon formation at 7033 ft, i.e., 50°C, 22.1 MPa (Senel & Chugunov, 2013). Sample pH and ionic strength were previously calculated for this pressure with representative minerals that comprise the Mt. Simon sandstone using the Geochemist Workbench React model (Botto et al.., 2017). An ionic strength of 5.135, and pH values between 3.4 and 4.8 were obtained depending on whether quartz, K-feldspar, illite, or hematite was considered the mineral phase in equilibrium.

During aging, CO_2 bubbles were periodically released from a 19-gauge needle below the sample, and became trapped on the sample's bottom surface. Images of CO_2 bubbles on the surface were recorded with a CCD camera (Guppy F-038C NIR) through a 16 mm zoom lens (Fujinon) set to time lapse capture. Experiments were run for ten days or nine weeks for sample aging. After each experiment, the view cell was taken apart, cleaned, dried, and reassembled to avoid the buildup of impurities which could lead to hysteresis.

Images were analyzed for CO_2 contact angle with ImageJ software using the axisymmetric drop shape analysis plugin (Rasband, 2016; Stalder, Kulik, Sage, Barbieri, & Hoffmann, 2006). At least 20 bubbles were averaged for each measurement day. By convention, contact angle is measured through the densest fluid phase, so in this work the contact angle represents the angle through the brine from the solid surface to the CO_2/brine interface.

Microscopy and Spectroscopy Methods

A Wyko NT 9100 Optical Profilometer was used to measure the surface roughness of each sample before and after aging. The data was collected using a 5X lens with a 0.55x field of view and set to different scan ranges for each sample, from 40 μm to 360 μm, depending on the roughness of the surface. The roughness parameter, r, defined as the ratio of the three-dimensional surface area over the two-dimensional areal projection, was calculated using Vision software.

A Leica DM 2500 compound light microscope with a Nikon camera was used in brightfield mode to image thin sections of core samples before and after aging for visualization of grain composition and clay coatings. Images used no polarized light filters and were adjusted to reflect true color. Images were taken with an exposure time of 10 ms.

A JEOL JSM-6490LV scanning electron microscope (SEM) coupled with energy dispersive spectroscopy (EDS) was used to analyze the surface of sandstone samples before and after aging to identify changes in surface morphology, mineral grain exposure, and clay coatings. The samples were non-conductive, so SEM was used in low-vacuum mode. Elemental composition determined by EDS was related to mineralogy by the chemical formula for individual minerals, e.g., a 1:2 atomic ratio of Si to O indicated quartz, SiO_2. Mineralogy of other materials was not as straightforward due to the high quantity of clays and weathering. Potassium feldspar, or K-feldpsar, $KAlSi_3O_8$, was determined by elemental composition of K=Al ± 2%. Due to large substitutions and variance within clays, such as illite, $(K,H_3O)(Al,Mg,Fe)_2(Si,Al)_4O_{10}[(OH)_2 \cdot nH_2O]$, and

smectite, $(Na,Ca)_{0.33}(Al,Mg)_2(Si_4O_{10})[(OH)_2 \cdot nH_2O]$, differentiating specific clay minerals was not possible with SEM-EDS (Barthelmy, 2014). All clays were considered together, with approximate identification of clays as 6% K and 9% Al, with the appellation of 'iron-rich' added if Fe content was greater than 4% of total atomic composition at that point. Mineralogical maps for thin sections were created using Photoshop edge detection and Ilastik software. Percent mineral contributions were determined through ImageJ threshold analysis.

An external X-ray diffraction (XRD) instrument was used to measure the mineralogical composition of the Mt. Simon sandstone before and after aging. Approximately 1 g of each sample was ground to a fine powder with a mortar and pestle before being sent to Premier Oilfield Laboratories for analysis.

Geomechanical Methods

Mt. Simon samples before and after aging were tested for fracture toughness and scratch hardness using a scratch test setup developed for reservoir rock analysis (Akono & Ulm, 2012; Sun, Aman, & Espinoza, 2016). The set up includes a moving stage onto which the sample was clamped between two acrylic spacers in a stainless-steel vice tightened with a screw. A diamond-tipped stylus with loads of 3.17 kg or 5.67 kg was then lowered into a fixed position so that it is in contact with the sample surface. An Arduino-controlled motor moved the stage, while the load cell recorded the frictional force created by the scratch and transmits it to the computer. Each sample was scratched for 3 mm. Scratch tests were performed when the Mt. Simon was completely dry, as well

as after being saturated with brine by submerging for 20 minutes to ensure entry into pore spaces. The latter was done to better represent clay plasticity in the Mt. Simon sample. A schematic of the scratch test apparatus is shown in Figure 3.

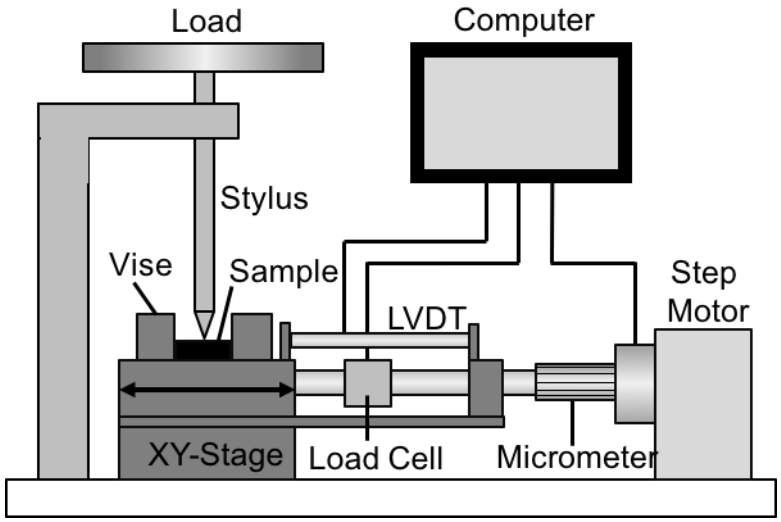

Figure 3: Geomechanical Scratch Test Apparatus.

Scratch width is correlated to the known shape of the diamond stylus to determine scratch depth. From Equations 1 and 2, the fracture toughness (K_c) and scratch hardness ($H_{scratch}$) of the studied material is determined (Akono & Ulm, 2012):

$$K_c = \frac{F_T}{\sqrt{2pA}} \quad [\text{MPa m}^{1/2}] \qquad \text{(Equation 1)}$$

$$H_{scratch} = \frac{kF_V}{w^2} \text{ [GPA]} \qquad \text{(Equation 2)}$$

For these equations, F_T is horizontal force, F_V is vertical force (constant), $2pA$ is the shape function of the indenter, k is a geometric constant, w is scratch width, and v is translation velocity (constant). A detailed explanation of scratch analysis is given in Results.

Results

Effects of Aging on Geochemical Alteration of the Mount Simon Sandstone

Contact angle values for the Mt. Simon sandstone over nine weeks of aging in CO_2-saturated brine at 20 MPa and 60°C are shown in Figure 4. The contact angle results for individual minerals that comprise the Mt. Simon sandstone, i.e., hematite, hematite-coated illite, K-feldspar and quartz, under the same conditions were previously determined (Botto et al., 2017) and are shown for comparison. A full table of the contact angle values is in Table A2.

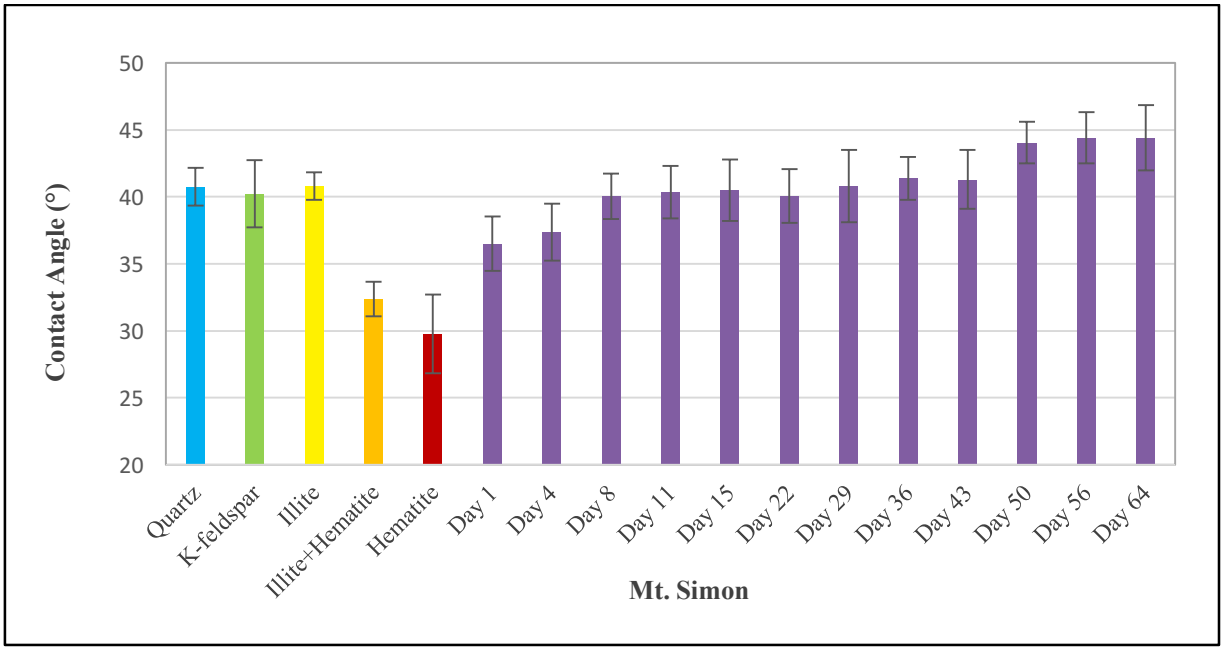

Figure 4: Contact angle values for Mt. Simon sandstone over nine weeks of aging in a CO_2-saturated brine at 20 MPa and 60°C, with contact angle values for primary minerals comprising the Mt. Simon sandstone (i.e., quartz, K-feldspar, hematite-coated illite, and hematite) in CO_2-saturated brine for reference. Values for the individual minerals are from Botto et al. (2017).

The results show that the contact angle for CO_2 on the Mount Simon sandstone was initially 36.5° ± 2.01°, and then rose during the first 8 days to 40.04° ± 1.7°. The contact angle remained relatively constant from Day 8 to 43, rose to 44.06° ± 1.56°, and then remained relatively constant for the next three weeks. Botto et al. (2017) previously modeled one-day contact angle values on the Mount Simon sandstone under similar conditions, and determined that contact angles are a function of surface roughness and mineralogy. Yoksoulian et al. (2013) demonstrated that CO_2 saturated brine can dissolve and/or remove illite clays from the Mt. Simon sandstone surface. As shown in Figure 6, contact angle values for hematite and hematite+illite are lower than those for Mt. Simon sandstone before aging, while those for quartz, K-feldspar, and illite are greater. The trend of increasing contact angle values with aging suggests Fe-rich illite clays may have been removed from the Mt. Simon sandstone surface, exposing more quartz and K-feldspar. The 64-day contact angle for the Mt. Simon is higher than quartz, K-feldspar, or pure illite alone, and suggests increasing surface roughness.

Microscopic and Spectroscopic Characterization of the Mt. Simon Sandstone

SEM images and EDS spectra were taken of the Mt. Simon samples before and after each experiment. SEM images before and after ten days of aging are shown in Figure 5. Illite and illite-smectite (hereafter referred to as clay) are identified by their morphology; they appear as light, interwoven flakes in between large grains (Keller, Reynolds, & Inoue, 1986) with the large grains being quartz and K-feldspar based on mineralogical characterization. An image of clay morphology is given in the Appendix

(Figure A1). The initial sample surface appears flat, and clay seems to fill pores and cement grains together. The aged surface has much less clay present on grain surfaces and pore spaces. The EDS spectra support the SEM observations. They indicate the connective, almost fibrous material between larger grains is clay, and that with aging an increased amount of pure SiO_2 and $KAlSi_3O_8$ are exposed at the surface. The full EDS spectrum and quantitative analysis is given in the Appendix (Figure A2).

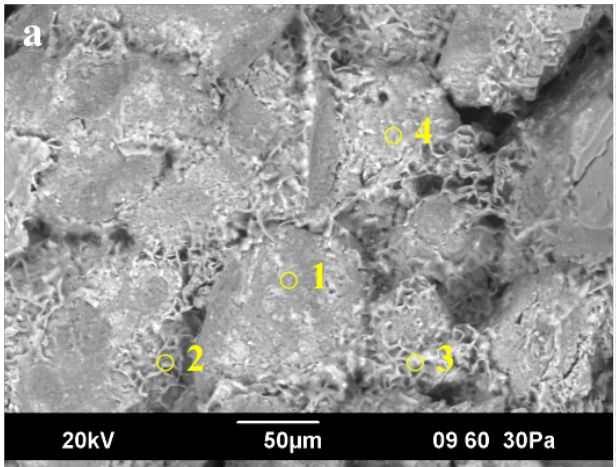

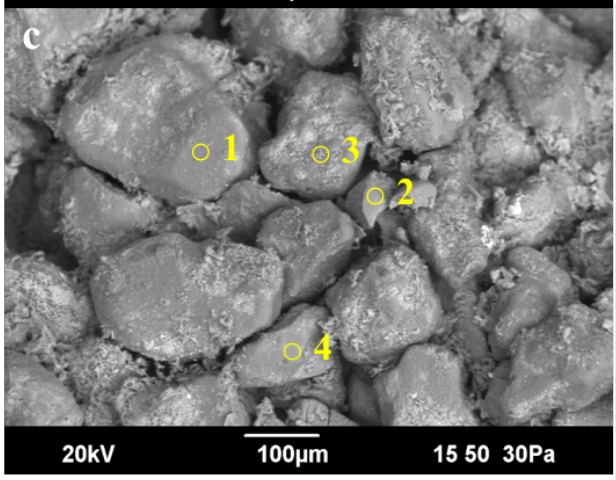

b	At%			
	1	2	3	4
O	39.32	30.81	43.12	54.25
Na	2.16	3.19	3.75	1.20
Mg	1.36	0.70	1.67	0.57
Al	5.50	8.48	10.63	9.00
Si	36.44	21.13	21.40	25.72
Cl	7.85	18.14	12.45	1.91
K	2.50	3.86	3.19	5.47
Ca	2.27	5.50	2.74	0.44
Fe	2.60	8.19	1.05	1.34
	Quartz	**Fe-clay**	**Clay**	**Clay**

d	At%			
	1	2	3	4
O	44.86	42.26	39.88	40.73
Na	0.93	0.65	1.22	0.5
Mg	-	-	-	-
Al	2.60	9.70	6.37	4.04
Si	58.08	32.56	38.49	47.84
Cl	1.90	2.48	3.99	2.46
K	1.42	9.93	3.06	1.46
Ca	1.51	0.8	1.64	1.17
Fe	2.61	1.62	5.36	1.79
	Quartz	**K-feldspar**	**Fe-clay**	**Quartz**

Figure 5: SEM images of Mt. Simon sample. (a) before aging and (c) after aging for ten days. Elemental Quantification and Mineral identification of grains and clays from SEM images (b) before aging and (d) after aging for ten days. Percentages of aluminum and potassium, described as clay, are reduced on the quartz.

SEM images of the Mt. Simon sandstone after nine weeks of aging are shown in Figures 6 and 7. As with samples aged ten days, there are markedly less clays between the larger grains after nine weeks. There are also locations where connective clay coatings are present that appear out of focus (due to being at a different depth of view in SEM), and also torn. This is attributed to surface grains being lost and the underlying clay that originally held grain to the rock matrix being exposed. The loss of grains is likely due to clays dissolving at the grain boundaries and larger grains falling away from the weakened matrix due to gravity. An image is given in the appendix of the reactor with grains present on the bottom of the interior (Figure A3).

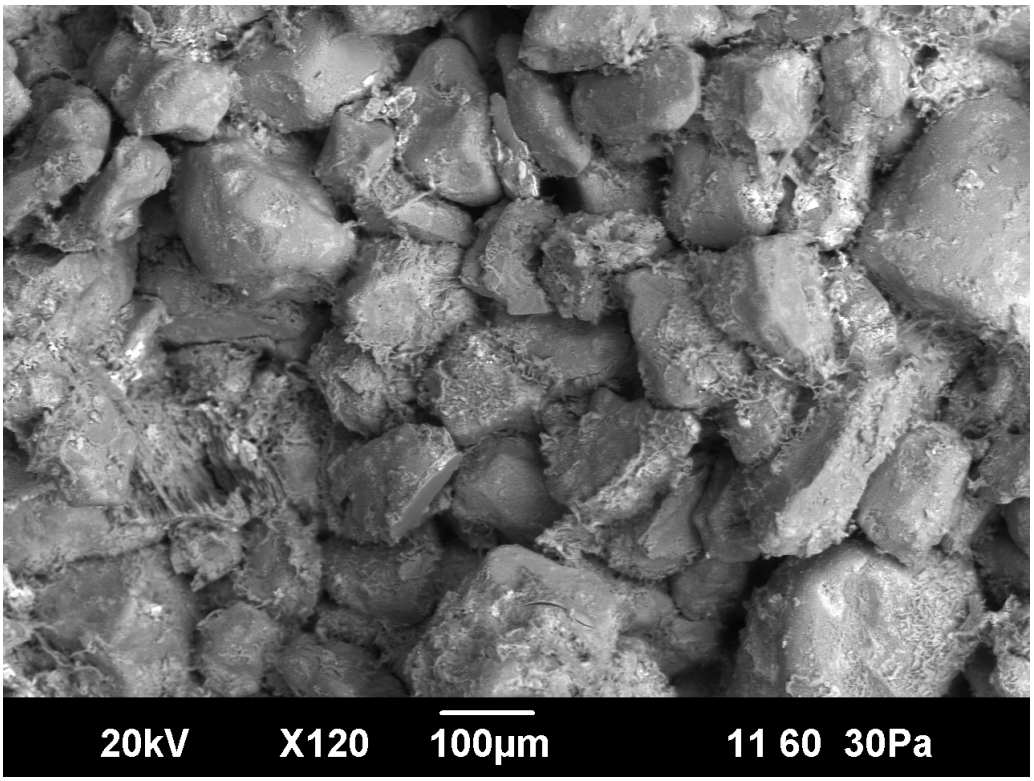

Figure 6: SEM images of Mt. Simon sample after aging for nine weeks. Connective illite/smectite clays are more limited, but still present. The overall surface is more heterogeneous.

Enlarged SEM images of two locations in the aged sample with corresponding EDS results are presented in Figure 7. The torn clays are seen visually as long, thin fibers in 7a, with characteristic high aluminum to potassium ratios in Figure 7b. A weathered K-feldspar grain is shown in Figure 7c. This mineral is also susceptible to dissolution during extended aging (Wigand et al., 2008) and after nine weeks it appears that some dissolution of these grains occurred. Aluminum is extracted into solution which can then precipitate as new clays (Wigley et al., 2013), which is shown in Figure 7d.

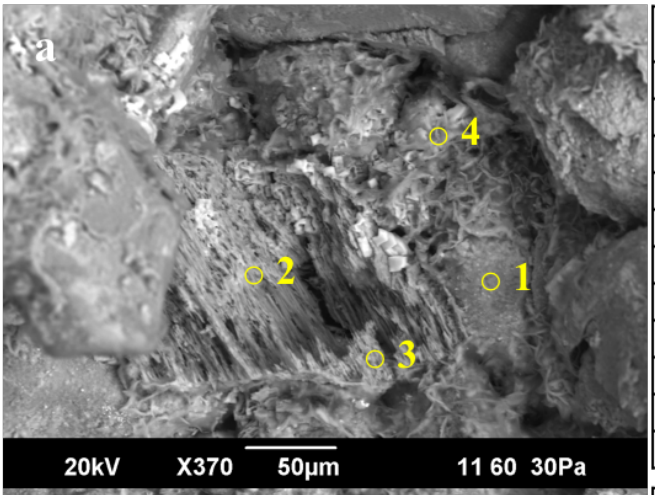

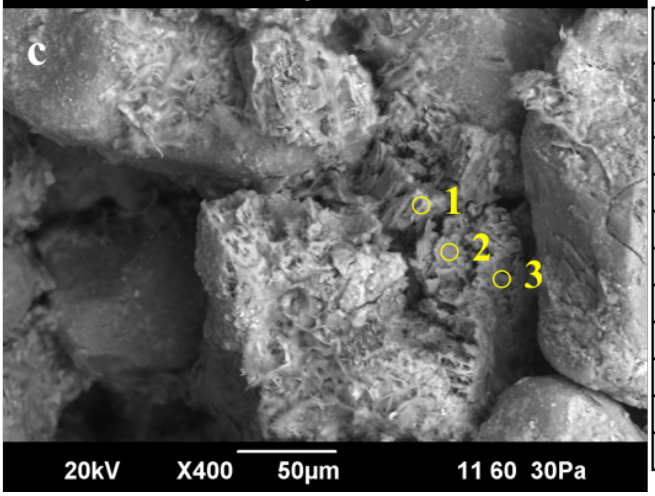

b	At%			
	1	2	3	4
O	43.23	48.19	48.33	48.02
Na	-	1.67	1.38	1.38
Mg	-	1.23	0.8	0.43
Al	3.0	7.85	9.14	8.38
Si	50.55	29.71	28.84	28.2
Cl	1.48	4.19	3.69	4.80
K	1.73	4.30	4.78	4.17
Ca	-	-	-	-
Fe	-	2.86	3.03	4.61
	Quartz	**Clay**	**Clay**	**Fe-clay**

d	At%		
	1	2	3
O	50.3	43.8	34.9
Na	1.2	0.6	0.7
Mg	1.23	0.3	0.5
Al	9.77	8.2	11.5
Si	17.3	28.3	36.9
S	1.4	2.1	1.6
K	7.5	14.0	12.2
Ca	0.6	0.9	0.7
Fe	0.8	1.8	1.2
	Clay	**K-feldspar**	**K-feldspar**

Figure 7: Elemental Quantification and Mineral identification of grains and clays from SEM images after aging for nine weeks. (a) Enlarged view of the torn clays in lower left of Figure 8, possibly indicating loss of grains. (b) EDS indicates torn fibers are clays near quartz grains. (c) Fractured K-feldspar grain with clay coatings. (d) EDS confirms the weathered grain is K-feldspar with reduced aluminum content from weathering, with new precipitated clay on site 1.

Standard 30-micron thin sections before and after aging were analyzed using optical microscopy and are shown in Figure 8. Purely by visual inspection, quartz grains are smooth and K-feldspar grains are textured. Clay and iron oxides are indicated by the brown coatings around larger grains. These continuous clay coatings around large grains are consistent with image analysis from Yoksoulian et al. (2013). SEM-EDS was used to

confirm the identify of minerals in the images, and a mineralogical map was created using Photoshop edge detection and Ilastik software. Percent mineral contributions were determined through ImageJ threshold analysis and are presented in Table 1. The pre- and post-aging mineral maps clearly show that before aging there is a uniform coating of clay and iron oxides on individual grains, while after aging the clay coatings are significantly more uneven; several large areas of clay coat full grain surfaces so that the individual grain cannot be determined, which causes the increase in clay from 19.6% to 29.3%. There was also a significant reduction in K-feldspar from 18.7% to 6.8%. Some of this percent loss is likely due to dissolution, but other apparent loss is due to precipitation of clays onto the K-feldspar; there are several grains visible in the optical images that could not be identified due to the limited penetration depth of EDS. SEM with accompanying EDS for the initial and aged thin sections is shown in Figure 9. The clay coatings that remain after aging have higher concentrations of aluminum and calcium than in the initial sample. These are weathering byproducts of the dissolution of K-feldspar ($KAlSi_3O_8$) and calcite ($CaCO_3$). Minimal change occurred for percentages of quartz and pore space. This measure of pore space does not consider the porosity of the clays, and takes what could be a thin film as filling the entire pore area. Therefore, an increase in porosity is likely, as seen in previous literature (Yoksoulian et al., 2013), but that was not quantified in this study.

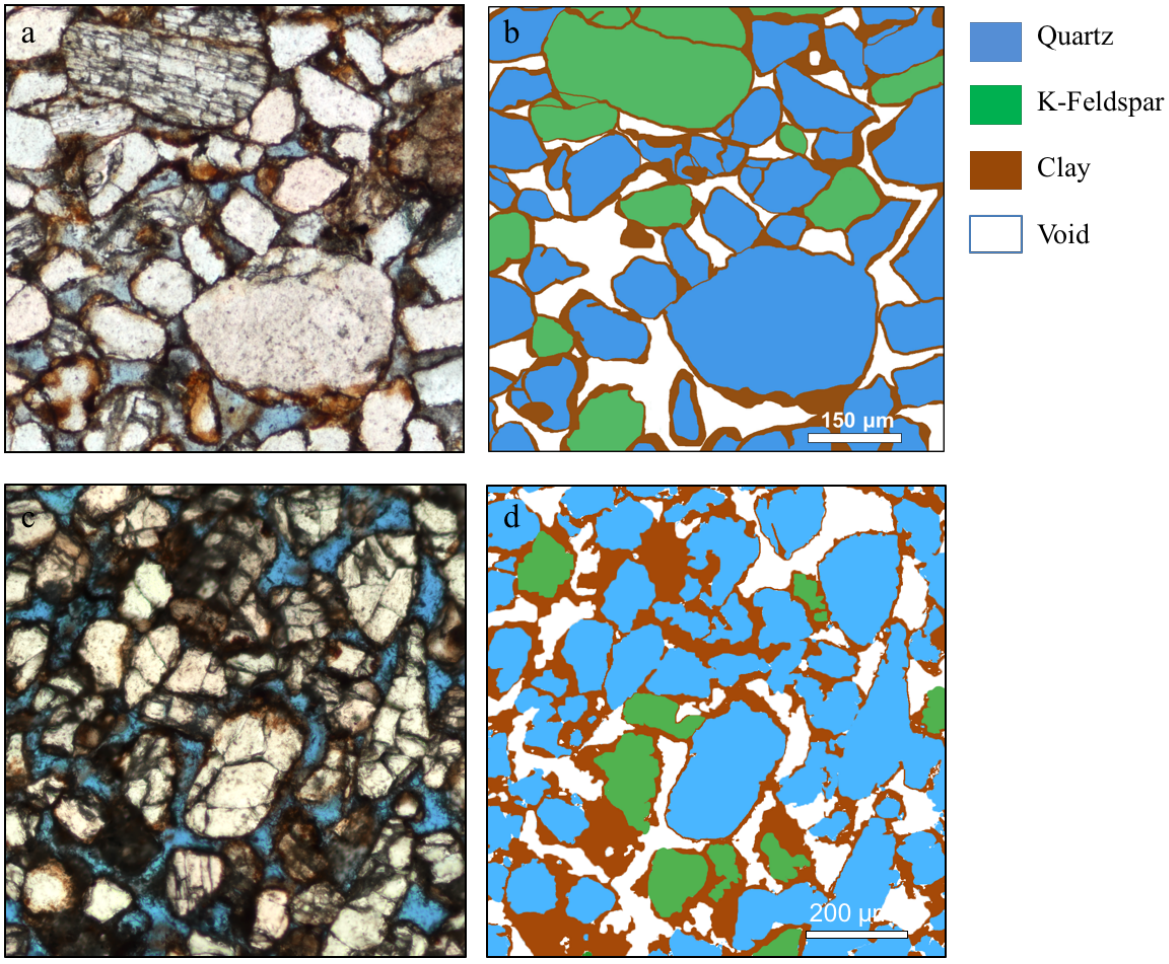

Figure 8: Optical thin sections and mineralogical maps for (a,b) initial Mt. Simon sandstone and (c,d) aged sample. Mineralogical maps were made through (b) Photoshop edge detect and (d) Ilastik software.

	Quartz	**K-feldspar**	**Clay**	**Void**
Initial	45.8%	18.7%	19.6%	15.9%
Aged	46.5%	6.8%	29.3%	17.4%

Table 1: Relative areal percentages of minerals and clays based upon thin sections of initial sample and aged sample. Percentages were found through ImageJ threshold analysis.

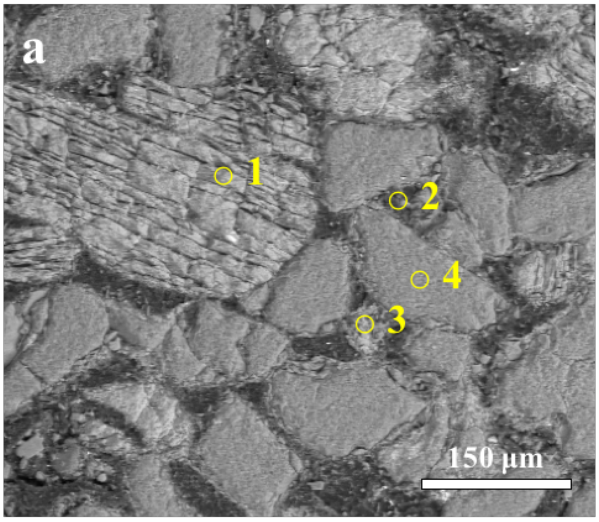

b	At%			
	1	2	3	4
O	47.97	52.07	41.77	50.98
Na	1.05	1.00	1.10	0.48
Mg	-	-	-	-
Al	9.98	6.76	11.37	1.73
Si	32.26	34.06	33.66	45.42
Cl	0.43	2.04	0.89	0.25
K	7.76	2.72	5.71	0.75
Ca	0.40	0.78	0.66	0.29
Fe	0.17	0.58	4.84	0.11
	K-feldspar	**Clay**	**Al,Fe-clay**	**Quartz**

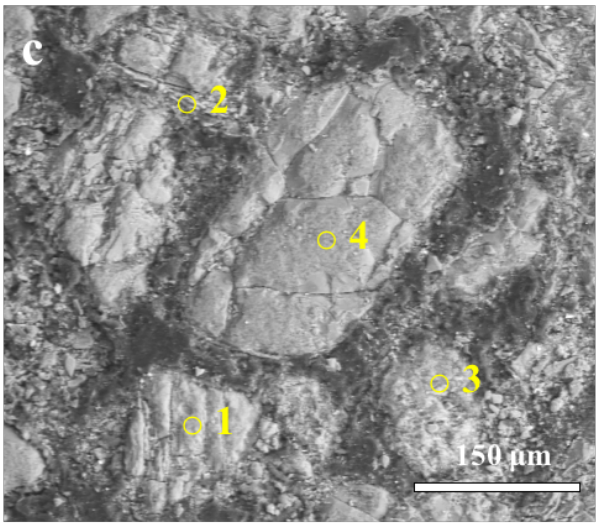

d	At%			
	1	2	3	4
O	40.49	48.56	34.80	45.72
Na	1.42	3.01	0.37	0.25
Mg	1.23	2.23	0.61	0.29
Al	11.31	10.04	15.31	1.73
Si	34.34	25.78	37.35	50.78
Cl	-	0.75	-	-
K	9.82	3.73	7.41	0.45
Ca	0.91	1.66	3.33	0.43
Fe	0.49	4.24	0.82	0.35
	K-feldspar	**Al,Fe-Clay**	**Al,Ca-Clay**	**Quartz**

Figure 9: Elemental Quantification and Mineral identification of grains and clays from SEM images of the thin sections of Mt. Simon sandstone made before and after aging. (a) SEM image of initial sample thin section. (b) EDS shows quartz, K-feldspar, clay, and Fe-clay. (c) SEM image of aged sample thin section. (d) EDS of several points on map show clays with higher aluminum and calcium content than noted previously.

Effects of Aging on Surface Roughness

The Mt. Simon sandstone surface roughness was evaluated using an optical profilometer, and representative images before and after aging are shown in Figure 10. The imaging software was used to calculate a roughness parameter, r, which is the three-

dimensional surface area over the corresponding two-dimensional projection (Nosonovsky, 2007). The pre-aged sample is characterized by r = 8.23 ± 0.71, while the post-aged sample has r = 17.067 ± 0.66 based on three averaged areas on the samples. The increased roughness following aging is likely a result of two factors: 1) dissolution of clay from the surface, creating wider pore spaces, and 2) weakening of clay leading to loss of grains. Without adequate clay cementation, quartz, K-feldspar, and other grains fall out of the sandstone matrix due to gravity and handling post-experiment; this is shown in Figure A3.

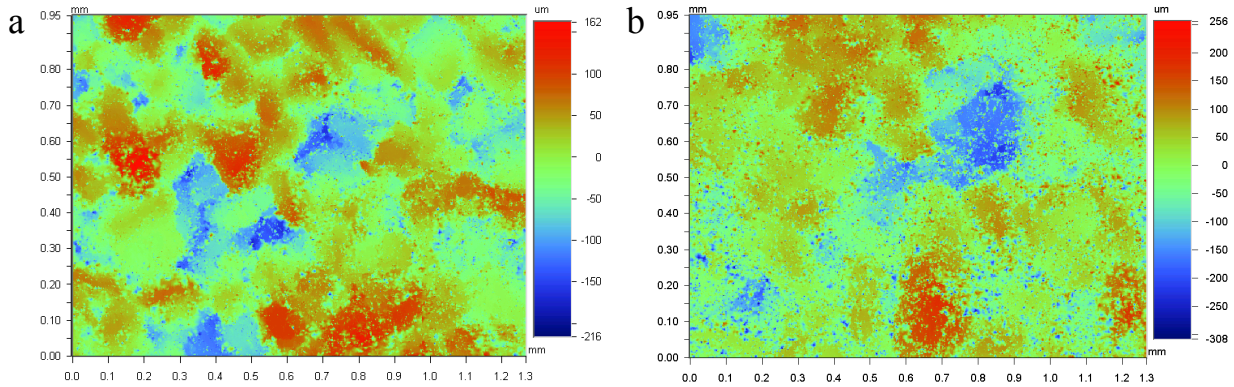

Figure 10: Profilometer images of the same sample before and after nine weeks of aging. The first set give a roughness index of r = 8.1 before aging and r = 17.3 after aging. Both images have different depth scales represented by color, from (a) -216 to 162 um and (b) -308 to 256 um.

Effects of Aging on Mineralogy

X-ray diffraction was used to further evaluate mineralogical changes in the Mt. Simon sandstone before and after aging, with results presented in Table 2. In both the pre- and post-aged Mt. Simon sandstone, the most abundant mineral species was quartz, and its percent abundance increased with aging. XRD provides the relative atomic

percent of each mineral in the reservoir sample, not the absolute amount of each mineral. Although quartz has a higher percentage in the aged sample; this does not mean that more quartz is present in the sample after aging, but more likely that other minerals were lost. The K-feldspar was the second largest mineral phase in initial and aged samples, but after aging it was reduced by 10% due to significant dissolution of the mineral in CO_2-saturated brine; this is consistent with the thin section results and literature studies on K-feldspar showing dissolution (Wigand et al., 2008).

The remaining minerals were present in much lower amounts, so the potential for error due to the heterogeneity of the Mt. Simon is likely. The relative percentage of carbonates (i.e., calcite, dolomite/ankerite, siderite) all decreased after aging; this is not surprising given their relatively high reactivity in low pH solutions (Deng et al. 2015; Wang et al. 2013). Similarly, the amounts of three clays (i.e., illite/smectite, kaolinite, and chlorite) all decreased. However, the amount of illite/mica increased. This could be related to the relative measurement, the heterogeneity of the material, or the dissolution of potassium feldspar: it is also reactive at low pH, and the release of cations from the K-feldspar could have precipitated into clays (Rosenqvist et al., 2014; Wigand et al., 2008). Finally, halite, or NaCl, was not present in the initial sample, but was present at 2.3% in the aged sample. All samples were only briefly rinsed with deionized water before drying to prevent clay removal post-experiment. NaCl likely precipitated from residual brine in the sample during drying.

Mineral	Formula	Initial % composition	Aged % composition	Type
Calcite	$CaCO_3$	2.1	0.0	Carbonate
Dolomite/ Ankerite	$Ca(Fe,Mg,Mn)(CO_3)_2$	0.5	0.4	Carbonate
Siderite	$FeCO_3$	0.3	0.1	Carbonate
Quartz	SiO_2	76.5	85.7	Tectosilicate
Orthoclase	$KAlSi_3O_8$	17.3	7.2	Tectosilicate
Illite/mica	$(K,H_3O)(Al,Mg,Fe)_2(Si,Al)_4O_{10}[(OH)_2 \cdot n(H_2O)]$	1.1	3.6	Clay
Kaolinite	$Al_2Si_2O_5(OH)_4$	0.4	0.1	Clay
Chlorite	$(Mg,Fe)_3(Si,Al)_4O_{10}(OH)_2 \cdot (Mg,Fe)_3(OH)_6$	0.3	0.0	Clay
Illite/ smectite	$(Na,Ca)_{0.33}(Al,Mg)_2(Si_4O_{10})[(OH)_2 \cdot nH_2O]$	0.7	0.5	Clay
Halite	NaCl	0.0	2.3	Salt
Marcasite	FeS_2	0.6	0.1	Iron sulfide

Table 2: Mineralogical composition percentages by XRD before and after aging.

Effects of Aging on Geomechanical Properties

Hardness and fracture toughness were measured on pre- and post-aged Mt. Simon sandstone using a geomechanical scratch test. Images of raw and processed scratches in the Mt. Simon sandstone are shown Figure 11. The images are taken with a light source at a near 90° angle from the top and bottom to create shadows that define the edges of the scratch. Initial images are imported and a histogram of color values is used with a threshold selection to identify darker areas on the mineral, i.e., the scratch. From threshold images, trace sections are combined to create the scratch area, the perimeter, and finally, the scratch width.

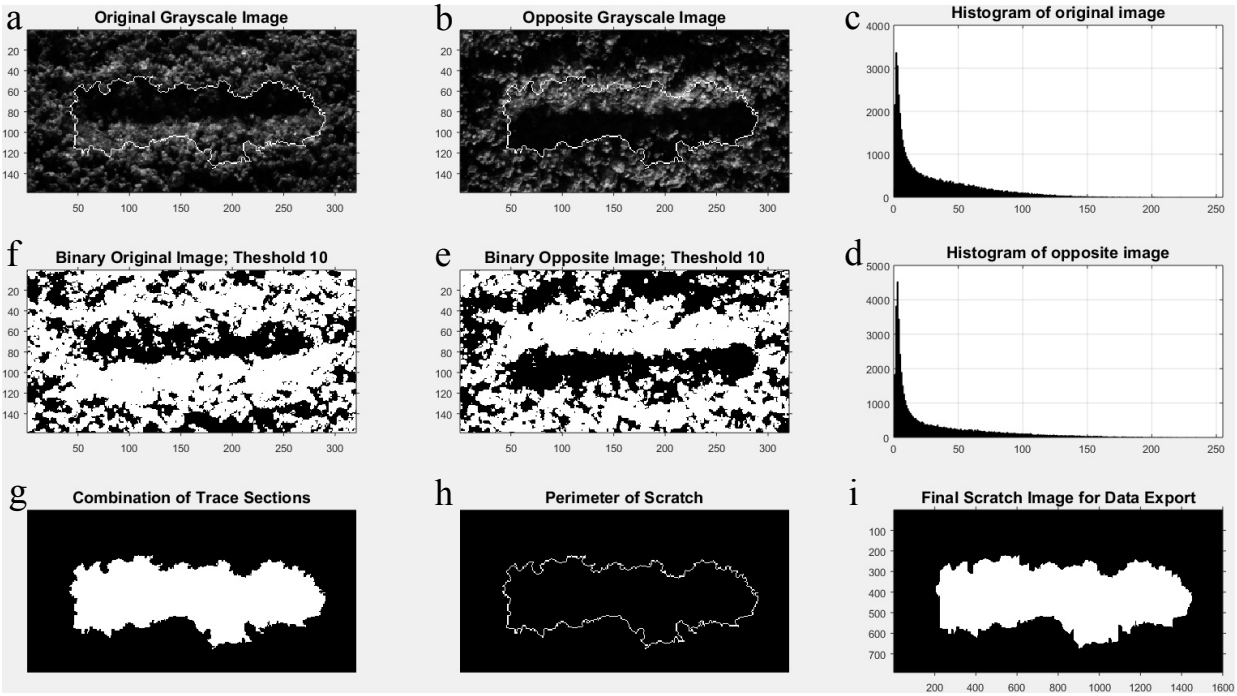

Figure 11: Matlab Image Analysis of dry, aged sample with 3.17 kg load scratch. (a,b) Initial images. (c,d) Histogram of color values. (e,f) Threshold color selection to identify scratch area (g) Total scratch area. (h) Scratch perimeter. (i) Image for Data Export.

After analysis of the scratch images and the transverse load, the fracture toughness and scratch hardness were calculated using equations 1 and 2. Scratch test results of initial and aged samples under both dry and brine-wet conditions are listed in Table 3. All results are averaged over the entire scratch length, and for at least two scratches on each sample. In comparing dry and wet samples, both initial and aged samples had reduced fracture toughness with wetting. Initial toughness was reduced by 84.9% when wetted, and aged toughness reduced by 34.3%. Initial scratch hardness was reduced by 70.5% when wetted, then aged hardness was reduced by 56.2%. The wet measurements have lowered mechanical properties due to the plasticity of clays in the presence of water. Water additionally swells smectite clays, reducing the electrostatic

interactions between layers and allowing slippage. These wet results are potentially more valid for the actual reservoir because the sandstone would always be saturated with natural brine; however, the reservoir pressure on geomechanical properties is not considered in this study.

The results also show there is a 63% reduction in fracture toughness and a 3.7% reduction in hardness for the dry sample after aging for nine weeks, indicating structural weakening. This is most likely due to the loss of cementing clays from the Mt. Simon sample during aging, which serve as the cementing agent for quartz and feldspar grains. Surprisingly, there is not a decrease in the hardness and fracture toughness for brine wet samples after aging for nine weeks. This is likely an issue with sample preparation for the scratch test. The first attempt at a scratch test after aging broke the sample in half, because the sample became more fragile with aging. To prevent structural failure, the 1/8 in thick sample disc was set on epoxy in an aluminum holder. The dry scratch was shallow, only penetrating approximately 1 mm into the sample. However, the wet scratch was deeper, approximately 2 mm into the sample, which may have reached the infiltrated epoxy holding the structural integrity of the sandstone. This would have given higher apparent values for mechanical properties. For this reason, the dry, aged sample data is considered reliable, but the wet, aged sample data provides an overestimate.

	Initial		**Aged**	
	Dry	Wet	Dry	Wet
Fracture Toughness ($MPa*m^{1/2}$)	1.7129 ± 0.56983	0.25734 ± 0.059626	0.63045 ± 0.15156	0.41399 ± 0.094446
Scratch Hardness (GPa)	0.071007 ± 0.035838	0.02095 ± 0.0049905	0.068326 ± 0.018709	0.029915 ± 0.0093934

Table 3: Geomechanical properties for Mt. Simon sandstone before and after aging at either dry or brine-saturated conditions.

Conclusions

The objectives of my thesis were to study the geochemical reactions that occur in a representative siliciclastic storage reservoir during CO_2 sequestration, and to determine if these reactions weaken reservoir rock. Over the course of nine weeks of aging in CO_2-saturated brine, multiple Mt. Simon sandstone samples were monitored for changes in contact angle as a surrogate for geochemical reactions. The contact angle increased from 36.5° ± 2.01° to 44.39° ± 2.45°, suggesting a loss of clay-iron oxide coatings, more surface exposure of quartz and feldspar grains, and possibly increasing surface roughness. The Mt. Simon sandstone was evaluated for mineralogy and surface roughness through a suite of microscopic and spectroscopic techniques before and after aging. SEM and EDS indicated the connective clay coatings were visibly reduced over the course of exposure to CO_2-saturated brine. Thin section analysis and XRD mineralogy confirmed the dissolution of K-feldspar and certain clays. Because of the high clay content observed in the aged sample thin section analysis, this research confirms that weathering byproducts precipitate as new clays under reservoir conditions. Profilometer imaging results indicate a 113% increase in surface roughness due to geochemical reactions during aging.

Geomechanical tests on Mt. Simon sandstone samples show that fracture toughness and hardness are reduced by 63% and 3.7%, respectively, on dry samples after aging, but no reduction was observed on wet samples after aging within the standard deviation. Initial fracture toughness was reduced by 84.9% when wetted, and aged sample toughness reduced by 34.3%. Initial scratch hardness was reduced by 70.5%

when wetted, then aged sample hardness was reduced by 56.2%. The wet measurements have lowered mechanical properties due to the plasticity of clays in the presence of water, which provides a challenge in measurement due to low sample integrity after aging, and requires further investigation.

The acidified brine resulted in the dissolution of carbonates, clays, and K-feldspar, increases in surface roughness, and a reduction in toughness. Further study is needed to probe the different reactions of specific minerals in conjunction with flow-through experiments.

The geomechanical alterations after aging Mt. Simon sandstone in CO_2 and brine are significant on a larger scale because the weakening of structure allows for easier fracturing when subject to applied stress, such as the increase in pore pressure from carbon sequestration. This can then be directly related to the microseismicity observed at the Mt. Simon site in Decatur, Illinois. In the 1.5 years before injection began, the site was monitored and only experienced 8 microsiesmic events unrelated to well drilling (Smith & Jaques, 2016). Over the course of three years during injection, the number of events averaged to more than 4 per day, often arranged in clusters at a variety of distances and depths from the injection well (Bauer, Carney, & Finley, 2016). Other sites of injection for enhanced oil recovery have only noted minimal microseismic events that can be directly tied to injection rates and pressure (Martínez-Garzón, Bohnhoff, Kwiatek, Zambrano-Narváez, & Chalaturnyk, 2013; Verdon, 2012; Whittaker et al., 2011). Understanding the geochemical reactions occurring at CO_2 injection sites is a key to

ensuring the safety of geological carbon sequestration so that future locations can be chosen with minimal risk of leakage.

Appendix

Chemical	Mass Added (g/L)	Concentration (mol/L)
NaCl	114.1598	1.9534
$CaCl_2$ H_2O	73.3672	0.6611
$MgCl_2$ H_2O	16.7293	0.1757
KCl	40.296	0.5405
KBr	1.117	0.0094
LiCl	0.1222	0.0029
$SrCl_2$ $6H_2O$	2.4343	0.0154
$Na_2B_4O_7$	0.7662	0.0038

Table A1: Synthetic brine recipe for the lower Mt. Simon formation.

	Experiment Date	Contact Angle (°)	Standard deviation
Quartz		40.76	1.40
K-feldspar		40.22	2.51
Illite		40.80	1.03
Illite+Hematite		32.37	1.29
Hematite		29.76	2.95
Mt. Simon	Day 1	36.5	2.01
	Day 4	37.35	2.125
	Day 8	40.04	1.70
	Day 11	40.346	1.955
	Day 15	40.5	2.30
	Day 22	40.058	2.02
	Day 29	40.8	2.70
	Day 36	41.39	1.6
	Day 43	41.29	2.19
	Day 50	44.06	1.56
	Day 56	44.4	1.93
	Day 64	44.394	2.45

Table A2: Equilibrium contact angle values for Mt. Simon endmembers and Mt. Simon after aging at 20 MPa.

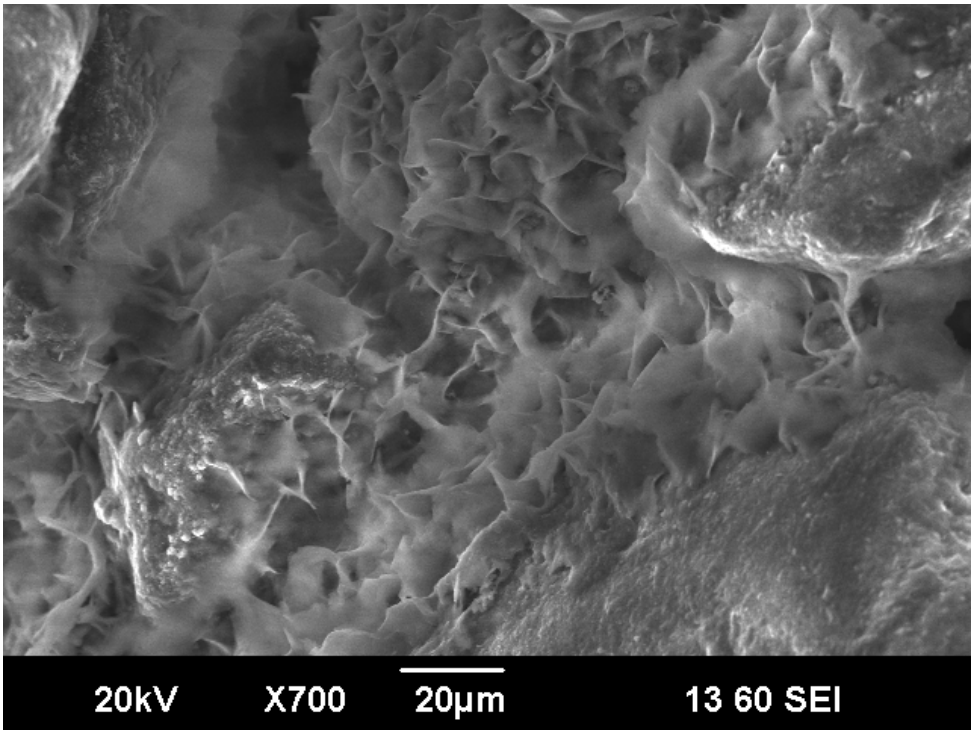

Figure A1: Morphology of illite-smectite clay, described as interconnected flakes, on quartz grains in the Mt. Simon.

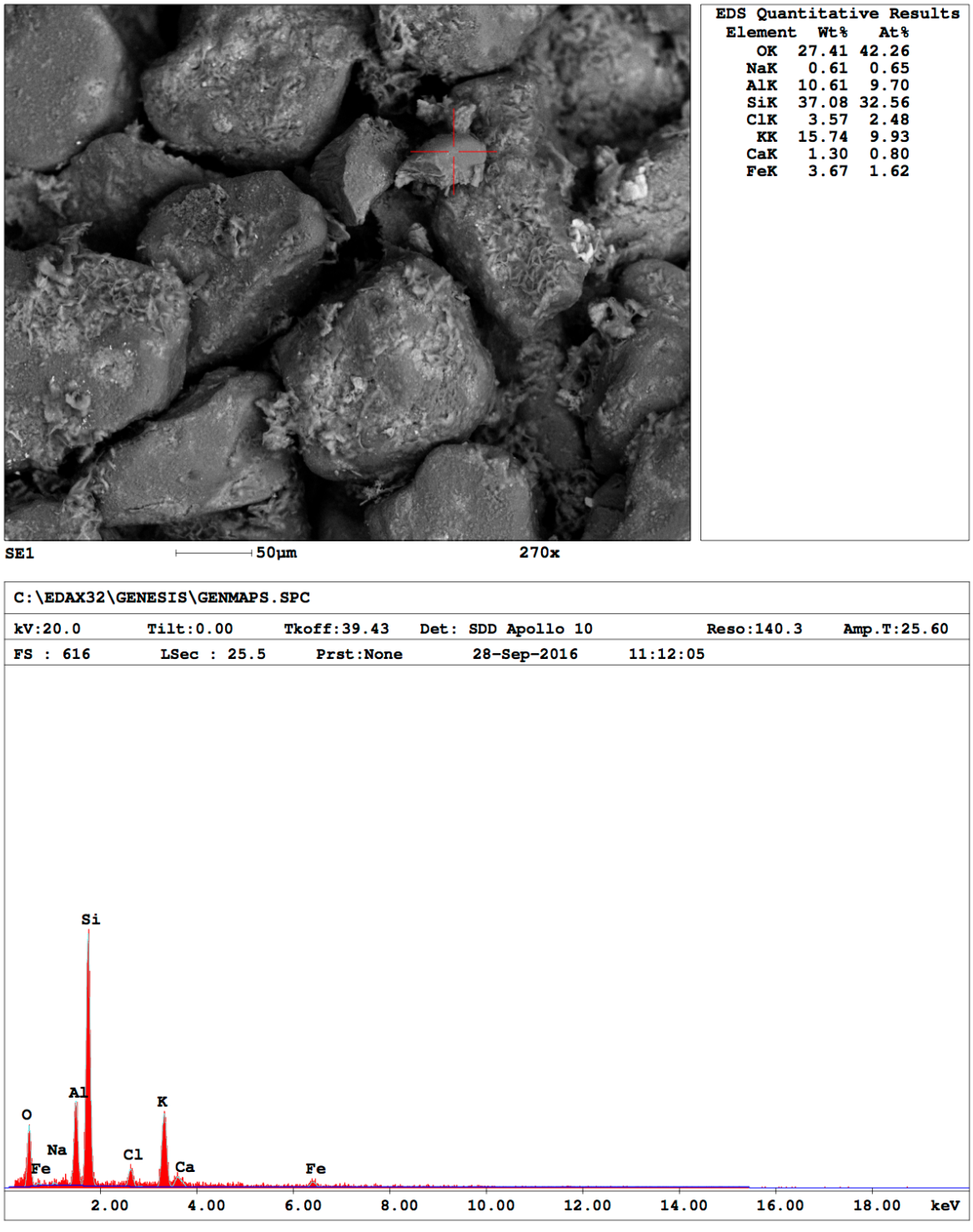

Figure A2: Example EDS Spectra with quantitative elemental analysis for Point 2 on Figure 8 bottom image. The equal values of aluminum and potassium helped to identify this grain as potassium feldspar, $KAlSi_3O_8$.

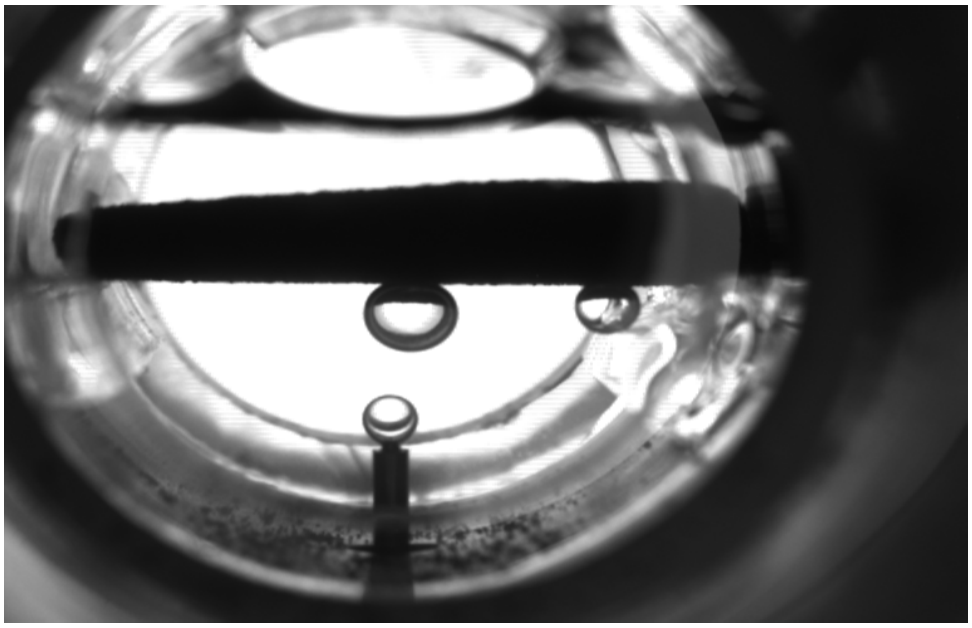

Figure A3: Mt. Simon Sandstone in view cell during aging with loose grains on the bottom.

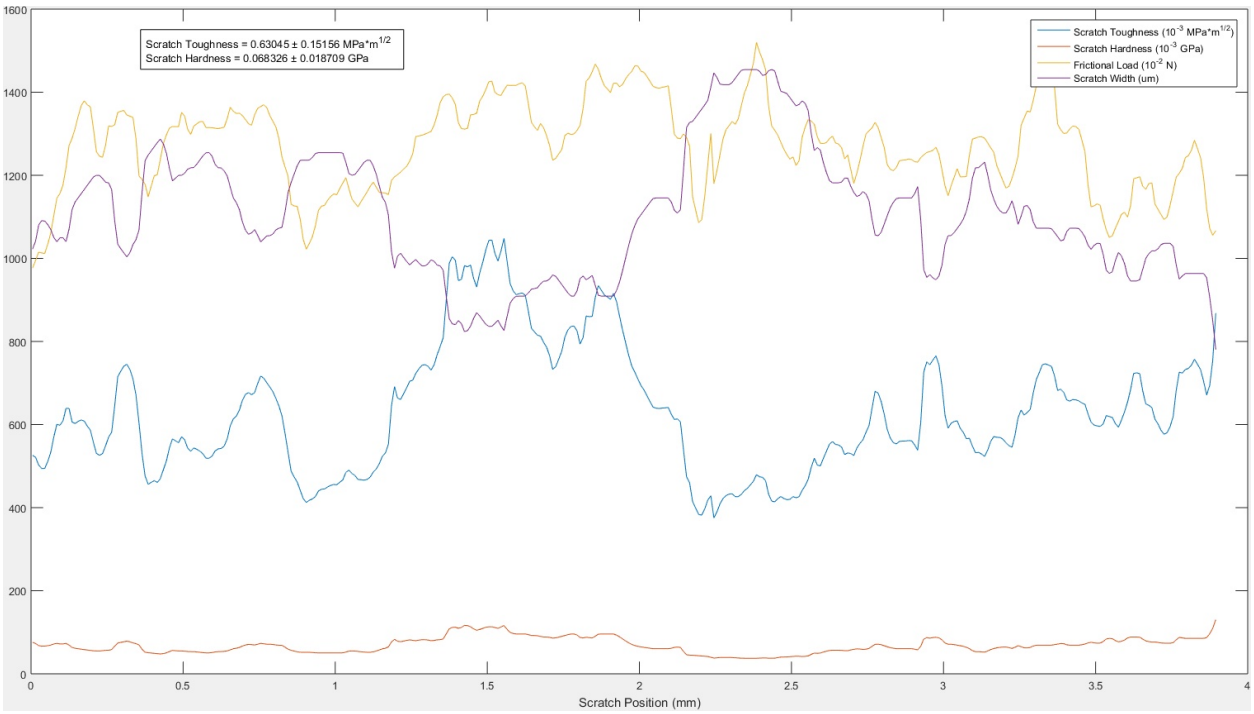

Figure A4: Matlab output chart of dry, aged sample with 3.17 kg load scratch. Frictional load (yellow) input from the load cell with scratch width (purple) determined from image analysis (Fig. 11). Calculation output yields toughness (blue) and hardness (red).

Bibliography

Akono, A.-T., & Ulm, F.-J. (2012). Fracture scaling relations for scratch tests of axisymmetric shape. *Journal of the Mechanics and Physics of Solids*, *60*(3), 379–390. https://doi.org/10.1016/j.jmps.2011.12.009

Amram, K., & Ganor, J. (2005). The combined effect of pH and temperature on smectite dissolution rate under acidic conditions. *Geochimica et Cosmochimica Acta*, *69*(10), 2535–2546. https://doi.org/10.1016/j.gca.2004.10.001

Barthelmy, D. (2014). Illite Mineral Data. Retrieved April 9, 2017, from http://webmineral.com/data/Illite.shtml#.WOltIFLMz-Y

Bauer, R. A., Carney, M., & Finley, R. J. (2016). Overview of microseismic response to CO2 injection into the Mt. Simon saline reservoir at the Illinois Basin-Decatur Project. *International Journal of Greenhouse Gas Control*, *54*(1), 378–388. https://doi.org/10.1016/j.ijggc.2015.12.015

Botto, J., Fuchs, S. J., Fouke, B. W., Clarens, A. F., Freiburg, J. T., Berger, P. M., & Werth, C. J. (2017). Effects of Mineral Surface Properties on Supercritical CO_2 Wettability in a Siliciclastic Reservoir. *Energy & Fuels*, acs.energyfuels.6b03336. https://doi.org/10.1021/acs.energyfuels.6b03336

Czernichowski-Lauriol, I., Rochelle, C., Gaus, I., Azaroual, M., Pearce, J., & Durst, P. (2006). GEOCHEMICAL INTERACTIONS BETWEEN CO2 , PORE-WATERS AND RESERVOIR ROCKS. *NATO Science Series IV Earth and Environmental Sciences*, *65*, 157–174. Retrieved from http://nora.nerc.ac.uk/866/1/NATO_Tomsk_final.pdf

Dawson, G. K. W., Sidiq, H., Pearce, J., Gao, J.-F., Golding, S. D., Rudolph, V., … Xing, H. (2013). ANLEC Project 3-1110-0101: Review of laboratory-scale geochemical and geomechanical experiments simulating geosequestration of CO2 in sandstone, and associated modelling studies. *Australian National Low Emissions Coal Research and Development, Manuka, ACT*. Retrieved from https://hub.globalccsinstitute.com/sites/default/files/publications/111836/review-laboratory-scale-geochemical-geomechanical-experiments.pdf

Deng, H., Fitts, J. P., Crandall, D., McIntyre, D., & Peters, C. A. (2015). Alterations of Fractures in Carbonate Rocks by CO2-Acidified Brines. *Environmental Science & Technology*, *49*(16), 10226–10234. https://doi.org/10.1021/acs.est.5b01980

Freiburg, J. T., Morse, D. G., Leetaru, H. E., Hoss, R. P., & Yan, Q. (2014). A Depositional and Diagenetic Characterization of the Mt. Simon Sandstone at the Illinois Basin - Decatur Project Carbon Capture and Storage Site, Decatur, Illinois, USA. *Illinois State Geological Survey, Prairie Research Institute*.

IPCC. (2005). *Carbon Dioxide Capture and Storage*. (B. Metz, O. Davidson, H. de Coninck, M. Loos, & L. Meyer, Eds.). Cambridge, New York: Cambridge University Press. Retrieved from https://www.ipcc.ch/pdf/special-reports/srccs/srccs_wholereport.pdf

IPCC, 2014. (2014). *Climate Change 2014: Synthesis Report. Contribution of Working Groups I, II, and III to the Fifth Assessment Report of the Intergovernmental Panel on Climate Change*. (Core Writing Team, R. K. Pachauri, & L. A. Meyer, Eds.). Geneva, Switzerland: IPCC. Retrieved from

http://epic.awi.de/37530/1/IPCC_AR5_SYR_Final.pdf

Kaven, J. O., Hickman, S. H., Mcgarr, A. F., & Ellsworth, W. L. (2015). Surface Monitoring of Microseismicity at the Decatur, Illinois, CO 2 Sequestration Demonstration Site. *Seismological Research Letters*, *86*(4). https://doi.org/10.1785/0220150062

Keller, W. D., Reynolds, R. C., & Inoue, A. (1986). MORPHOLOGY OF CLAY MINERALS IN THE SMECTITE-TO-ILLITE CONVERSION SERIES BY SCANNING ELECTRON MICROSCOPY. *Clays and Clay Minerals*, *34*(2), 187–197. Retrieved from http://www.clays.org/journal/archive/volume 34/34-2-187.pdf

Martínez-Garzón, P., Bohnhoff, M., Kwiatek, G., Zambrano-Narváez, G., & Chalaturnyk, R. (2013). Microseismic Monitoring of CO2 Injection at the Penn West Enhanced Oil Recovery Pilot Project, Canada: Implications for Detection of Wellbore Leakage. *Sensors*, *13*(9), 11522–11538. https://doi.org/10.3390/s130911522

Nosonovsky, M. (2007). On the Range of Applicability of the Wenzel and Cassie Equations. *Langmuir*, *23*(19), 9919–9920. https://doi.org/10.1021/LA701324M

Rasband, W. S. (2016). ImageJ. Retrieved April 9, 2017, from https://imagej.nih.gov/ij/

Rosenqvist, J., Kilpatrick, A. D., Yardley, B. W. D., & Rochelle, C. A. (2014). Feldspar dissolution at CO 2 -saturated conditions. In *EGU General Assembly*. Retrieved from http://wserv4.esc.cam.ac.uk/crius/wp-content/uploads/2014/04/Jorgen-Rosenqvist.pdf

Senel, O., & Chugunov, N. (2013). CO2 Injection in a Saline Formation: Pre-Injection Reservoir Modeling and Uncertainty Analysis for Illinois Basin – Decatur Project.

Energy Procedia, *37*, 4598–4611. https://doi.org/10.1016/j.egypro.2013.06.368

Smith, V., & Jaques, P. (2016). Illinois Basin – Decatur Project pre-injection microseismic analysis. *International Journal of Greenhouse Gas Control*, *54*, 362–377. https://doi.org/10.1016/j.ijggc.2015.12.004

Stalder, A. F., Kulik, G., Sage, D., Barbieri, L., & Hoffmann, P. (2006). A snake-based approach to accurate determination of both contact points and contact angles. *Aspects*, *286*, 92–103. https://doi.org/10.1016/j.colsurfa.2006.03.008

Sun, Y., Aman, M., & Espinoza, D. N. (2016). Assessment of mechanical rock alteration caused by CO2□water mixtures using indentation and scratch experiments. *International Journal of Greenhouse Gas Control*, *45*, 9–17. https://doi.org/10.1016/j.ijggc.2015.11.021

US EPA, O. (2016). Climate Change Indicators: U.S. Greenhouse Gas Emissions. Retrieved April 9, 2017, from https://www.epa.gov/climate-indicators/climate-change-indicators-us-greenhouse-gas-emissions

Verdon, J. P. (2012). *Microseismic Monitoring and Geomechanical Modelling of CO2 Storage in Subsurface Reservoirs*. https://doi.org/10.1007/978-3-642-25388-1

Wang, S., Edwards, I. M., & Clarens, A. F. (2013). Wettability Phenomena at the CO 2 −Brine−Mineral Interface: Implications for Geologic Carbon Sequestration. *Environmental Science and Technology*, *47*, 234–241. https://doi.org/10.1021/es301297z

Wang, X., Alvarado, V., Swoboda-Colberg, N., & Kaszuba, J. P. (2013). Reactivity of dolomite in water-saturated supercritical carbon dioxide: Significance for carbon

capture and storage and for enhanced oil and gas recovery. *Energy Conversion and Management*, *65*, 564–573. https://doi.org/10.1016/j.enconman.2012.07.024

Whittaker, S., Rostron, B., Hawkes, C., Gardner, C., White, D., Johnson, J., … Seeburger, D. (2011). A decade of CO2 injection into depleting oil fields: Monitoring and research activities of the IEA GHG Weyburn-Midale CO2 Monitoring and Storage Project. *Energy Procedia*, *4*, 6069–6076. https://doi.org/10.1016/j.egypro.2011.02.612

Wigand, M., Carey, J. W., Schütt, H., Spangenberg, E., & Erzinger, J. (2008). Geochemical effects of CO2 sequestration in sandstones under simulated in situ conditions of deep saline aquifers. *Applied Geochemistry*, *23*(9), 2735–2745. https://doi.org/10.1016/j.apgeochem.2008.06.006

Wigley, M., Dubacq, B., Kampman, N., & Bickle, M. (2013). Controls of sluggish, CO 2 -promoted, hematite and K-feldspar dissolution kinetics in sandstones. *Earth and Planetary Science Letters*, *362*, 76–87. https://doi.org/10.1016/j.epsl.2012.11.045

Yoksoulian, L. E., Freiburg, J. T., Butler, S. K., Berger, P. M., & Roy, W. R. (2013). Mineralogical alterations during laboratory-scale carbon sequestration experiments for the Illinois Basin. *Energy Procedia*, *37*(37), 5601–5611. https://doi.org/10.1016/j.egypro.2013.06.482